Reconstructing the shear modulus contrast of linear elastic and isotropic media in quasi-static ultrasound elastography

Elisabeth Brusseau[1], Lorena Petrusca[1], Elie Bretin[2], Pierre Millien[3] and Laurent Seppecher[4]

Abstract— This study focuses on the reconstruction of the shear modulus contrast in linear elastic and isotropic media, in quasi-static ultrasound elastography. The method proposed is based on the variational formulation of the equilibrium equations and on the choice of adapted discretization spaces to estimate the parameters of interest. Experimental results obtained with CIRS phantoms are presented, for which regions with different mechanical properties can be clearly identified in the stiffness contrast maps. Elastic modulus images collected with a shear-wave elastography technique from a clinical ultrasound scanner (Aixplorer) are also provided for comparison. Results show very similar values for the modulus ratios determined by the two elastography approaches.

I. INTRODUCTION

Elastography techniques have been introduced to supplement conventional imaging with information on the mechanical properties of biological tissues [1]. The quasi-static ultrasound approach analyzes the internal displacements and strains that tissues experience when they are subjected to compression [2], [3]. Although this technique is generally limited to strain imaging, its ability to distinguish regions differing in stiffness is recognized. Strain images, however, do not exactly reflect the variation in elastic modulus, as the stress distribution is not uniform.

Various approaches can be found in the literature for reconstructing the mechanical parameters or stiffness contrast in a medium [4]. Among the methods developed for quasi-static ultrasound elastography is the direct inversion, as proposed in [5] for example to recover the spatial distribution of the Young's modulus E in a 3D body. The method consists in substituting, in the equilibrium equations, the stress terms using the material constitutive law. Assuming that the Poisson's ratio is known and constant throughout the body, this results in equations where the unknowns are the spatial derivatives of E, divided by E. Values of E are then determined relative to a reference (e.g. the surface Young's modulus) which, when known, leads to moduli in kPa. Because of its simplicity, direct inversion is an attractive method. Nevertheless, it requires differentiating the displacement and strain fields, which dramatically affects the results if the displacements are initially noisy.

Mapping the Young's modulus can also be formulated as an optimization problem, where the modulus values are iteratively varied until mimimizing an error between the displacements or strains determined by solving the forward problem and those measured experimentally [6], [7]. In practice, difficulties can be encountered for clinical applications, because some boundary information is needed.

Recently, the use of machine learning has been reported. In [8] for instance, Hoerig *et al.* investigated the mechanical properties of media under quasi-static load. Their approach consists in learning the stress-strain relationship, to then deduce the parameters of interest. However, a set of force-displacement measurements has to be provided as input data.

As significant differences in the mechanical properties are expected between healthy and pathological tissues, stiffness contrast assessment is of interest for diagnosis. This explains the use of strain ratios in quasi-static elastography, even though they only partially reflect the modulus contrast [9]. In shear-wave elastography also, the stiffness ratio appears as a useful parameter, able to differentiate benign from malignant lesions [10], [11]. The present study focuses on shear modulus contrast reconstruction of linear elastic and isotropic media in quasi-static elastography. In a recent paper [12], we introduced a first 2D method to reconstruct this contrast from the knowledge of 2D displacement fields. This method, based on a problem weak formulation, used a classical finite element discretization with a triangular mesh, as well as a total variation (TV) regularization applied on the searched parameters. Performing various tests has led us to modify this approach, which now uses a hexagonal mesh with triangular sub-mesh, while the TV regularization has been removed. The new method is fully described below, and the improvement in the results illustrated with simulated data. Experimental results are also presented and compared with those from a shear-wave elastography technique.

II. METHOD

This study focuses on the reconstruction of shear modulus maps up to a multiplicative constant, in linear elastic and isotropic media, from displacement fields obtained in quasi-static ultrasound elastography. Because the data generally available in ultrasound imaging are 2D images, the 2D problem has been investigated, i.e. recovering the spatial distribution of the shear modulus $\mu(x, y)$ up to a multiplicative constant (x and y being the spatial coordinates), from 2D displacement fields $\boldsymbol{u}(x, y)$ estimated in a 2D domain Ω. Let us consider a linear elastic and isotropic medium. The constitutive equation of such a medium is:

[1]Univ Lyon, INSA-Lyon, Université Claude Bernard Lyon 1, UJM Saint-Etienne, CNRS, Inserm, CREATIS UMR 5220, U1294, France
[2]Institut Camille Jordan, INSA de Lyon, UCBL, Lyon, France
[3]Institut Langevin, CNRS UMR 7587, ESPCI Paris, PSL Research University, Paris, France
[4]Institut Camille Jordan, Ecole Centrale de Lyon, UCBL, Lyon, France

$$\sigma_{ij} = 2\mu\varepsilon_{ij} + \lambda\delta_{ij}\varepsilon_{kk} \qquad (1)$$

where λ with μ are the Lamé parameters, σ_{ij} and ε_{ij} the components of the stress and strain tensors, σ and $\mathcal{E}$, respectively, δ_{ij} the Kronecker delta, and ε_{kk}, the trace of $\mathcal{E}$. The displacement field $\boldsymbol{u}$ inside Ω resulting from a quasi-static elastography experiment, satisfies the equilibrium equations. Neglecting the body forces, these equations write

$$\nabla \cdot \sigma = \mathbf{0}, \qquad (2)$$

and combining (1) and (2) gives

$$\nabla \cdot \left(2\mu\mathcal{E}(\boldsymbol{u})\right) + \nabla(\lambda\nabla \cdot \boldsymbol{u}) = \mathbf{0}, \qquad (3)$$

with $\mathcal{E}(\boldsymbol{u}) := \left(\nabla\boldsymbol{u} + (\nabla\boldsymbol{u})^\top\right)/2$ the strain tensor, and $\nabla\cdot$ and ∇, the divergence and gradient operators, respectively.

A. Weak formulation

The method proposed is based on a variational formulation of (3). As the unknown parameters λ and μ are discontinuous, we look for them as elements of the parameter space $M := L^2(\Omega)$. Moreover, test functions $\boldsymbol{v} \in V := H_0^1(\Omega, \mathbb{R}^2)$ are chosen such that they vanish at the domain boundary ($\partial\Omega$), as no information on the applied forces is available.

$$H_0^1(\Omega, \mathbb{R}^2) := \\ \left\{\boldsymbol{v} \in L^2\left(\Omega, \mathbb{R}^2\right) \mid \nabla\boldsymbol{v} \in L^2\left(\Omega, \mathbb{R}^{2\times 2}\right), \ \boldsymbol{v}|_{\partial\Omega} = \mathbf{0}\right\}. \qquad (4)$$

Then, multiplying (3) by $\boldsymbol{v}$, taking the integral and finally integrating by parts, leads to

$$\int_\Omega 2\mu\mathcal{E}(\boldsymbol{u}) : \mathcal{E}(\boldsymbol{v}) + \int_\Omega \lambda(\nabla \cdot \boldsymbol{u})(\nabla \cdot \boldsymbol{v}) = 0 \quad \forall\boldsymbol{v} \in V, \ (5)$$

with $\mathcal{E}(\boldsymbol{u}) : \mathcal{E}(\boldsymbol{v}) := \sum_{ij} \mathcal{E}(\boldsymbol{u})_{ij}\mathcal{E}(\boldsymbol{v})_{ij}$.

B. Finite element method

To build a finite dimensional system of equations, we approach the two function spaces M and V by finite dimensional discretization subspaces $M_h \subset M$ and $V_h \subset V$ where $h > 0$ is a parameter of discretization. Let us denote $\left(e_1^{M_h}, \dots e_{\dim M_h}^{M_h}\right)$ a basis of M_h and $\left(e_1^{V_h}, \dots e_{\dim V_h}^{V_h}\right)$ a basis of V_h. With $\mu = \sum_j \mu_j e_j^{M_h}$ and $\lambda = \sum_j \lambda_j e_j^{M_h}$, it follows from (5) that

$$\mathcal{A}\boldsymbol{\mu} + \mathcal{B}\boldsymbol{\lambda} = \mathbf{0}, \qquad (6)$$

with

$$\begin{cases} \mathcal{A}_{ij} & := \int_\Omega 2e_j^{M_h}\mathcal{E}(\boldsymbol{u}) : \mathcal{E}(e_i^{V_h}) \\ \mathcal{B}_{ij} & := \int_\Omega e_j^{M_h}(\nabla \cdot \boldsymbol{u})(\nabla \cdot e_i^{V_h}), \end{cases}$$

$\boldsymbol{\lambda} := (\lambda_1, \dots, \lambda_{\dim M_h})^\top$ and $\boldsymbol{\mu} := (\mu_1, \dots, \mu_{\dim M_h})^\top$.

C. Choice of discretization spaces

The choice of a pair of discretization spaces M_h and V_h is difficult, and is certainly the key question of this inversion. Here, we have found that a very efficient discretization technique that has excellent numerical stability is the honeycomb space discretization. The domain $\Omega \subset \mathbb{R}^2$ is covered by a hexagonal honeycomb tiling of edge size $h > 0$,

$$\overline{\Omega} = \bigcup_{k=1}^{N_h} \overline{\Omega_k^h}. \qquad (7)$$

A sub-discretization of Ω is also performed using an adapted equilateral triangulation $\{\tau_k^h\}$. We choose the parameter approximation space M_h as the class $\mathcal{P}_0\left(\{\Omega_k^h\}\right)$ of functions that are constant in each hexagon. Moreover, we define V_h as a subset of the classical $\mathcal{P}_1\left(\{\tau_k^h\}, \mathbb{R}^2\right)$ finite element class. More precisely, for each intersection node p_i of three adjacent hexagons, we define φ_i as the unique function that is linear in each triangle and that satisfies $\varphi_i(p_i) = 1$, and cancels at any other nodes of the triangular sub-mesh. Let us now define the vector-valued test functions

$$\boldsymbol{e}_{ik}^{V_h}(x, y) := \varphi_i(x, y) \begin{bmatrix} \delta_{1k} \\ \delta_{2k} \end{bmatrix} \quad k = 1, 2, \qquad (8)$$

for i such that p_i is an intersection node of three hexagons. The space V_h is the subspace of V generated by these functions.

D. Solution computation

The problem is reduced to finding nonzero solutions of

$$\mathcal{M}\boldsymbol{p} = \mathbf{0}, \qquad (9)$$

with $\mathcal{M} := \begin{bmatrix} \mathcal{A} & \mathcal{B} \end{bmatrix}$ and $\boldsymbol{p} := \begin{bmatrix} \boldsymbol{\mu} \\ \boldsymbol{\lambda} \end{bmatrix}$. More precisely, the problem to be solved is:

$$\underset{\boldsymbol{p}}{\operatorname{argmin}} \|\mathcal{M}\boldsymbol{p}\|_2^2 \qquad (10)$$

subject to some constraints, such as bound constraints since the parameters to be determined are necessarily positive values, or the values of $\boldsymbol{p}$ on the domain boundary equal to 1. In practice, the solution computation is peformed using the *CVX Matlab toolbox* [13], [14].

E. Use of multiple data

Using not only one, but multiple displacement data $\boldsymbol{u}^1, \dots, \boldsymbol{u}^n$, can be easily performed with our approach. For each displacement field $\boldsymbol{u}^\ell$, the corresponding matrix $\mathcal{M}^\ell$ is built, as explained above. The multiple data problem is then formulated as in (10), but with $\mathcal{M} := \begin{bmatrix} \mathcal{M}^1 \dots \mathcal{M}^n \end{bmatrix}^\top$. The use of multiple data is adapted to our application since sequences of displacement fields during medium compression are typically obtained in elastography.

III. RESULTS

A. Contribution of the new approach

To illustrate the contribution of the new method compared with the initial one, an example of results is displayed in Fig. 1, obtained with a 2D simulated medium. This medium consists of a circular inclusion embedded in a homogeneous background material. The inclusion-to-background shear modulus ratio is equal to 3 (Fig. 1a). Medium compression was simulated using *Comsol Multiphysics* [15] and the resulting displacements were used to estimate the stiffness contrast. Shear modulus contrast maps computed with the method using a triangular mesh (Fig. 1b), a triangular mesh and the TV regularization (former method, Fig. 1c), and with
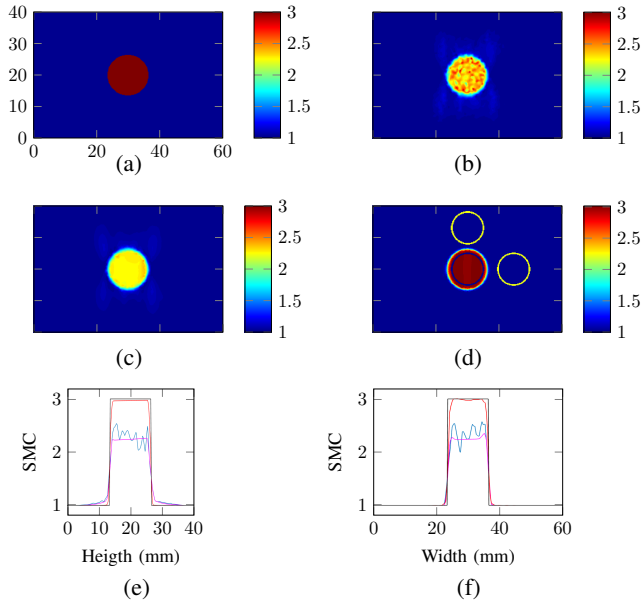
Fig. 1. Shear modulus contrast (SMC, without unit) maps obtained with the 2D simulated medium. (a) Theoretical map (axes are in mm), and maps reconstructed with (b) a triangular mesh and without TV regularization, (c) using triangular mesh and TV regularization (former method), and (d) with the new method. In (d), the ROI selection for inclusion-to-background stiffness ratio computation is also shown. (e) and (f), profiles along the vertical and horizontal lines crossing the center of the inclusion, respectively, for the theoretical map (black), and the maps obtained with the triangular mesh only (blue), the former method (magenta), and the new method (red).
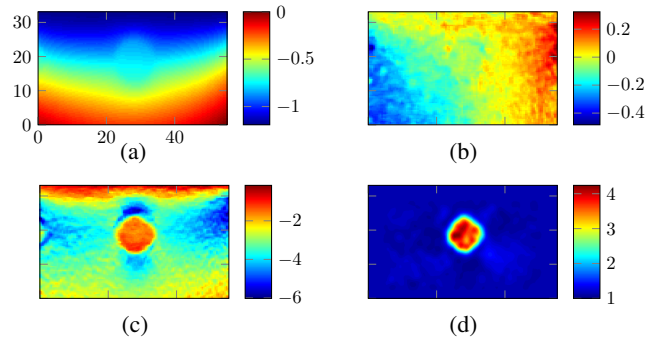

Fig. 2. Results obtained with the CIRS model 049, Type IV inclusion (case #1). (a) axial and (b) lateral displacement (in mm), (c) axial strain (in %), and (d) reconstructed shear modulus contrast map. In (a), axes are in mm.

the new approach (Fig. 1d), are shown. We can observe that the former method (Fig. 1c) leads to an image where the inclusion is clearly revealed with a well-defined boundary. As expected, the TV regularization resulted in a smoothing of the map, and more particularly of the inclusion which appears now uniform. However, compared with the theoretical map (Fig. 1a), a lower contrast can also be noted. With the new approach (Fig. 1d), similar comments can be made regarding the inclusion boundary and smooth appearance, but the stiffness ratio is this time very close to the one expected. For a more quantitative assessment of the results, inclusion-to-background stiffness ratios are here provided, by selecting regions of interest (ROIs) inside the inclusion and the background, and computing the ratio of their mean values. The region selection is performed identically for the three estimated maps, and for each case, two ratios are computed, from two different ROIs in the background (as shown in Fig. 1d). These ratios are 2.29 and 2.37 for the method using the triangular mesh, 2.20 and 2.25 for the former method, and 2.98 (twice) for the proposed approach, the latter being in perfect agreement with the theory. Finally, two profiles along the vertical and horizontal lines crossing the center of the inclusion are also displayed (Fig. 1(e,f)), for a more complete illustration of the results.

B. Experimental results

Three examples of results obtained from phantom experiments are detailed below.

1) Phantom specifications and data acquisition: Two CIRS phantoms (models 049 and 059, Computerized Imag-

ing Reference Systems, Norfolk, VA, USA) were used. The CIRS model 049 is a parallelepiped-shaped medium, with several spherical inclusions of different stiffnesses inside. For this phantom, two regions were scanned. Both contained a 10-mm in diameter inclusion, whose Young's modulus is 81 kPa for the first region (Type IV inclusion, case #1), and 47 kPa for the other one (Type III inclusion, case #2). The Young's modulus of the background material is 26.5 kPa. The second phantom – model 059 – has an external shape that mimics a female breast, and contains several spherical inclusions that are stiffer than the surrounding medium. The Young's moduli of the inclusions and the background are 43.3 kPa and 13 kPa, respectively. The region examined included a single inclusion (case #3). Note that the phantom specifications were all provided by the manufacturer.

Radiofrequency (RF) ultrasound images were collected during typical quasi-static elastography experiments, where the operator cautiously compressed the medium with the probe. Data were acquired with an *Ultrasonix* ultrasound scanner equipped with a L14-5W/60 linear array transducer. The sampling frequency was 40 MHz. Finally, displacements were estimated from RF data, using our method previously developed for strain imaging [16], and regularized before reconstruction.

2) Shear modulus contrast reconstruction: The results are presented in Figs. 2-4 with, for each case, an example of the estimated displacement fields, of the axial strain and the reconstructed shear modulus contrast map. All the reconstructions were performed using multiple (five) displacement fields. As the reconstructed maps are obtained up to a multiplicative constant, they were divided by their minimum value before display, and are therefore without unit.

In all the cases examined, the inclusion is clearly brought out in the modulus contrast map. These maps are in agreement with what is expected, even though some variations can remain in regions supposed to be mechanically homogeneous. For each case, two inclusion-to-background stiffness ratios were computed. These ones are 3.2 and 3.3 for case #1, 1.5 and 1.5 for case #2, and 2.1 and 2.2 for case #3. Compared with those given by the manufacturer (81/26.5; 47/26.5; 43.3/13), these ratios are relatively close, except for
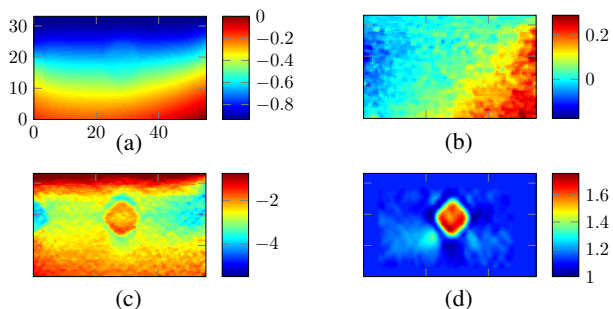
Fig. 3. Results obtained with the CIRS model 049, Type III inclusion (case #2). (a) axial and (b) lateral displacement (in mm), (c) axial strain (in %), and (d) reconstructed map. In (a), axes are in mm.
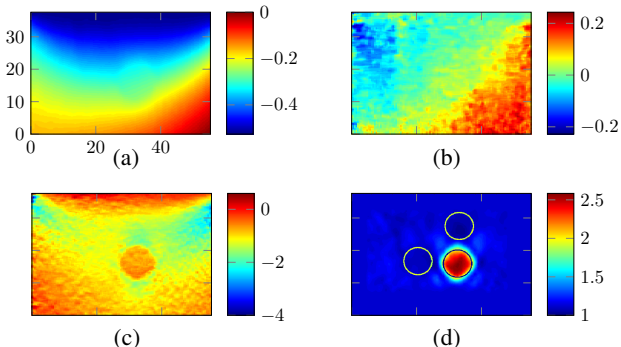

Fig. 4. Results obtained with the breast phantom (case #3). (a) axial and (b) lateral displacement (in mm), (c) axial strain (in %), and (d) reconstructed map, with an illustration of ROI selection. In (a), axes are in mm.
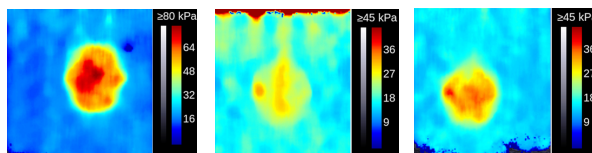

Fig. 5. Young's modulus images (in kPa) obtained with the Aixplorer ultrasound scanner. From left to right: model 049 - Type IV inclusion (case #1), model 049 - Type III inclusion (case #2), and model 059 (case #3).
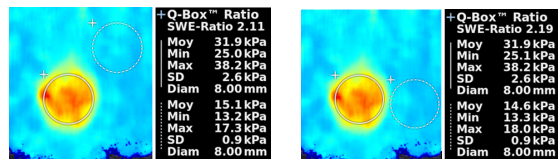

Fig. 6. Illustration of modulus ratios provided by the Aixplorer. The region analyzed is the one of the breast elastography phantom (case #3).

case #3, for which much lower values are obtained. To more deeply analyze and assess these results, a comparison with a shear-wave elastography technique was performed, using an *Aixplorer* ultrasound scanner (SuperSonic Imagine, Aix-en-Provence, France) equipped with a SL15-4 transducer. This system provides images of the Young's modulus E, proportional to μ, which allows for the stiffness ratios from both techniques to be directly compared. Elastograms are presented in Fig. 5, along with an illustration of ROI selection for inclusion-to-background stiffness ratio computation in Fig. 6. These ratios are here found to be 3.4 and 3.6 for case #1, 1.4 and 1.6 for case #2, and 2.1 and 2.2 for case #3. It is remarkable that, although different in their approach, the two elastography techniques provide very similar ratios. Moreover, the same unexpected low values for case #3 are observed, and will require additional work to be fully understood.

IV. CONCLUSIONS

In this study, a method for reconstructing the contrast in the shear modulus within a medium in quasi-static ultrasound elastography has been presented. The initial experimental results are encouraging, with inclusions that are clearly revealed in the new maps, and modulus ratios comparable to those provided by a clinical ultrasound scanner. Future work will be dedicated to further assessing and improving the method. In particular, this approach was developed in 2D as the ultrasound data available were 2D images. However, actual displacements and strains are 3D, and the 2D vs 3D

problem will be particularly investigated.

REFERENCES

[1] K. J. Parker, M. M. Doyley, and D. J. Rubens, "Imaging the elastic properties of tissue: the 20 year perspective," *Physics in Medicine and Biology*, vol. 56, no. 1, pp. R1–R29, 2011.

[2] J. Ophir, I. Céspedes, et al., "Elastography: a quantitative method for imaging the elasticity of biological tissues," *Ultrasonic Imaging*, vol. 13, no. 2, pp. 111–134, 1991.

[3] T. Varghese, "Quasi-static ultrasound elastography," *Ultrasound Clinics*, vol. 4, no. 3, pp. 323–338, 2009.

[4] M. M. Doyley, "Model-based elastography: a survey of approaches to the inverse elasticity problem," *Physics in Medicine and Biology*, vol. 57, no. 3, pp. R35–R73, 2012.

[5] N. Nitta and T. Shiina, "A method of tissue elasticity estimation based on three-dimensional displacement vector," *Japanese Journal of Applied Physics*, vol. 39, no. 5S, pp. 3225–3229, 2000.

[6] M. M. Doyley, P. M. Meaney, and J. C. Bamber, "Evaluation of an iterative reconstruction method for quantitative elastography," *Physics in Medicine and Biology*, vol. 45, no. 6, pp. 1521–1540, 2000.

[7] R. A. Baldewsing, J. A. Schaar, et al., "Assessment of vulnerable plaque composition by matching the deformation of a parametric plaque model to measured plaque deformation," *IEEE Transactions on Medical Imaging*, vol. 24, no. 4, pp. 514–528, 2005.

[8] C. Hoerig, J. Ghaboussi, and M. F. Insana, "Physics-guided machine learning for 3-D quantitative quasi-static elasticity imaging," *Physics in Medicine and Biology*, vol. 65, no. 6, pp. 065011, 2020.

[9] N. Cho, W. K. Moon, et al., "Sonoelastographic strain index for differentiation of benign and malignant nonpalpable breast masses," *Journal of Ultrasound in Medicine*, vol. 29, no. 1, pp. 1–7, 2010.

[10] W. A. Berg, D. O. Cosgrove, et al., "Shear-wave elastography improves the specificity of breast US: the BE1 multinational study of 939 masses," *Radiology*, vol. 262, no. 2, pp. 435–449, 2012.

[11] F. W.-F. Au, S. Ghai, et al., "Diagnostic performance of quantitative shear wave elastography in the evaluation of solid breast masses: determination of the most discriminatory parameter," *AJR*, vol. 203, no. 3, pp. W328–W336, 2014.

[12] H. Ammari, E. Bretin, et al., "A direct linear inversion for discontinuous elastic parameters recovery from internal displacement information only," *Numerische Mathematik*, vol. 147, no. 1, pp. 189–226, 2021.

[13] M. Grant and S. Boyd, "CVX: Matlab software for disciplined convex programming, version 2.1," http://cvxr.com/cvx, 2014.

[14] M. Grant and S. Boyd, "Graph implementations for nonsmooth convex programs," in *Recent Advances in Learning and Control*, V. Blondel, S. Boyd, and H. Kimura, Eds., Lecture Notes in Control and Information Sciences, pp. 95–110. Springer-Verlag Limited, 2008.

[15] COMSOL Multiphysics, *www.comsol.com*, COMSOL AB, Stockholm, Sweden.

[16] E. Brusseau, V. Detti, et al., "In vivo response to compression of 35 breast lesions observed with a two-dimensional locally regularized strain estimation method," *Ultrasound in Medicine and Biology*, vol. 40, no. 2, pp. 300–312, 2014.